Construction of the RSS V3.2 Lower-Tropospheric Temperature Dataset from the MSU and AMSU Microwave Sounders

CARL A. MEARS AND FRANK J. WENTZ

Remote Sensing Systems, Santa Rosa, California

(Manuscript received 29 September 2008, in final form 11 February 2009)

ABSTRACT

Measurements made by microwave sounding instruments provide a multidecadal record of atmospheric temperature in several thick atmospheric layers. Satellite measurements began in late 1978 with the launch of the first Microwave Sounding Unit (MSU) and have continued to the present via the use of measurements from the follow-on series of instruments, the Advanced Microwave Sounding Unit (AMSU). The weighting function for MSU channel 2 is centered in the middle troposphere but contains significant weight in the lower stratosphere. To obtain an estimate of tropospheric temperature change that is free from stratospheric effects, a weighted average of MSU channel 2 measurements made at different local zenith angles is used to extrapolate the measurements toward the surface, which results in a measurement of changes in the lower troposphere. In this paper, a description is provided of methods that were used to extend the MSU method to the newer AMSU channel 5 measurements and to intercalibrate the results from the different types of satellites. Then, satellite measurements are compared to results from homogenized radiosonde datasets. The results are found to be in excellent agreement with the radiosonde results in the northern extratropics, where the majority of the radiosonde stations are located.

1. Introduction

Temperature sounding microwave radiometers flown on polar-orbiting weather satellites provide an important record of upper-atmosphere temperatures beginning with the Microwave Sounding Unit (MSU) on the *Television and Infrared Observation Satellite-N* (*TIROS-N*) satellite in 1978. In the following years, a series of eight additional MSU instruments provided a continuous record up to February 2004, when significant gaps developed in the data from the *National Oceanic and Atmospheric Administration-14* (*NOAA-14*) satellite, the last MSU. The MSU instruments made sounding measurements using 4 channels. Thermal emission from atmospheric oxygen constitutes the major component of the measured brightness temperature, with the maximum in the temperature weighting profile varying from near the surface in channel 1 to the lower stratosphere in channel 4. Interpretation of the MSU channel 2 data is complicated by the fact that a significant portion of the signal arises from the lower stratosphere, which cooled rapidly during the 1978–96 period. This part of the signal tends to partially cancel the warming signal from the troposphere, thus obscuring the results (Fu et al. 2004). To reduce the effects of stratospheric cooling, Spencer and Christy (1992) at the University of Alabama at Huntsville (UAH) developed a lower-tropospheric dataset by calculating a weighted difference of near-limb and near-nadir views for the MSU instrument. Their dataset has evolved significantly since its inception as new methods of making adjustments to reduce the effects of a number of calibration issues and time-varying biases have been developed (Christy et al. 2000, 2003). Fu et al. (2004) and Fu and Johanson (2005) developed an alternative approach for removing stratospheric influence by combining results from multiple MSU channels. Starting in 1998, the MSU instruments were superseded by a second series of instruments, the Advanced Microwave Sounding Units (AMSUs), which are also flown on polar-orbiting weather satellites (Goodrum et al. 2000). Recent versions of the UAH dataset include AMSU data; therefore, it is continually updated.

Because atmospheric temperature trends and their agreement (or lack thereof) with the predictions of climate models have important policy implications, it is

---

Corresponding author address: Carl A. Mears, Remote Sensing Systems, 438 First Street, Suite 200, Santa Rosa, CA 95401.
E-mail: mears@remss.com

DOI: 10.1175/2009JTECHA1237.1

important that several groups analyze the data from these satellites (Thorne et al. 2005a). To this end, we produced a second version of this dataset [Remote Sensing Systems version 2.1 (RSS V2.1)] using data from the MSU satellites (Mears and Wentz 2005). Because this version of lower-tropospheric dataset only included data from the MSU satellites, the dataset was accurate only to the end of 2003. After this time, there is a significant amount of missing data from the last MSU satellite, *NOAA-14*, that makes it difficult to extend the record further without using AMSU data.

In this paper, we describe the procedures we have used to merge data from channel 5 in the newer AMSU instruments (AMSU5) with data from channel 2 in the earlier MSU instruments (MSU2) to extend the lower-tropospheric record beyond 2004. In section 2, we provide more details about the two instruments, focusing on their differences. In section 3, we describe the methods we have used to construct and adjust the AMSU dataset so that it matches the MSU data as closely as possible. In section 4, we show the results of our procedure. In section 5, we compare our results to other estimates of tropospheric temperature change.

2. Description of the MSU and AMSU instruments

a. Swath geometry

Both MSU and AMSU are cross-track scanning radiometers that measure the upwelling brightness temperature at a number of different view angles as they scan the earth perpendicular to the satellite subtrack. MSU views the earth at 11 different viewing angles separated by 9.47°, yielding a range of view angles from 0.0° for the nadir view to 47.35° for the two views furthest from nadir (Kidwell 1998). On the earth's surface, this corresponds to earth incidence angles ranging from 0.0° to approximately 56.19°. MSU has a half-power beamwidth of 7.5°, corresponding to a nadir spot size on the earth of 110 km, expanding to 178 km × 322 km for the near-limb view resulting from the increased distance from the satellite and oblique incidence angle. The AMSU instruments have significantly higher spatial resolution, viewing the earth at 30 different viewing angles separated by 3.33°, with view angles ranging from 1.67° to 48.33° (Goodrum et al. 2000). These view angles correspond to earth incidence angles ranging from 1.88° to 57.22°. The half-power beamwidth of the AMSU instrument is 3.3°, yielding a nadir spot size of 48 km × 48 km, increasing to 80 km × 150 km for the near-limb views. Because the MSU lower-tropospheric dataset is constructed using a weighted difference of measurements made at different view angles, these differences in viewing geometry between the MSU and AMSU instruments complicate the merging procedure.

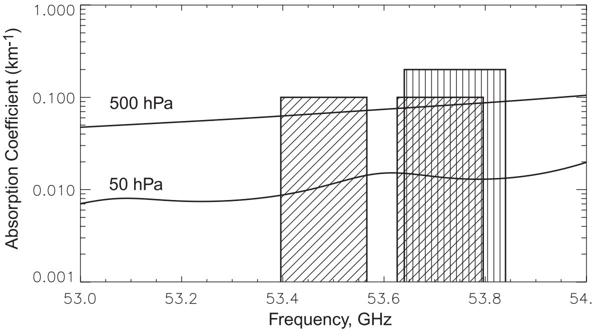

FIG. 1. Measurement bands for MSU channel 2 (vertical hatching) and AMSU channel 5 (diagonal hatching). Also plotted are the atmospheric absorption coefficients as a function of frequency for 500 and 50 hPa. Because the average of the absorptivity over the AMSU measurement bands is less than the corresponding average for the MSU measurement band, the AMSU temperature weighting function peaks closer to the surface for a given incidence angle.

b. Temperature weighting functions

AMSU5 is a double-sideband receiver that is sensitive to two sidebands centered at 53.71 and 53.48 GHz, each with a bandwidth of 0.17 GHz. MSU channel 2 (MSU2) is a single-sideband receiver centered at 53.74 GHz with a bandwidth of 0.20 GHz. Because (on average), ASMU5 uses a lower frequency than MSU2, the AMSU5 weighting function peaks nearer to the surface than the corresponding MSU weighting function for a given incidence angle. In Fig. 1, we plot the measurement bands for the two instruments, as well as the oxygen-absorption coefficient (Rosenkranz 1993) for the atmosphere at two representative pressures.

The brightness temperature T_b of the microwave radiation incident on the satellite is given by

$$T_b = W_S T(0) + \int_0^{\mathrm{TOA}} W(z) T(z)\, dz, \tag{1}$$

where W_s is the surface weight, $T(z)$ is the temperature at height z, $W(z)$ is the temperature weighting function, and the integral extends from the surface to the top of the atmosphere (TOA). The surface weight and the temperature weighting functions are dependent on the atmospheric absorption coefficient $\kappa(z)$ as a function of height z, the surface emissivity e_s, and the local zenith angle θ of the radiation path through the atmosphere. We consider oxygen and water vapor in these calculations. Under the assumption of specular reflection from the surface, W_s and $W(z)$ are given by

$$
\begin{aligned}
W_s &= e_s e^{-\tau(0,\infty)\sec\theta} \\
W(z) &= \sec\theta\{1 + (1 - e_s)[e^{-\tau(0,z)\sec\theta}]^2\}\kappa(z)e^{-\tau(z,\infty)\sec\theta},
\end{aligned}
\tag{2}
$$

where $\tau(z_1, z_2)$ is the zenith optical depth for a layer that extends in height from z_1 to z_2 (Ulaby et al. 1981). The temperature weighting function contains contributions from radiation emitted by each layer, which initially travels both in the upward and downward directions. The downward-travelling radiation propagates to the surface and reflects upward. Increasing the zenith angle causes the surface weight to be reduced and the temperature weighting function to move higher in the atmosphere. In Fig. 2, we plot temperature weighting functions for each view of MSU channel 2 and AMSU channel 5 for simulated land and ocean views using the *U.S. Standard Atmosphere, 1976* and an assumed relative humidity profile. These calculations were made using a radiative transfer model based on Rosenkranz (1993, 1998) and a model of the ocean surface developed by Wentz and Meissner (2000). For a given incidence angle, the AMSU channel 5 weighting function peaks several hundred meters closer to the surface, and the contribution of the surface is increased substantially relative to the corresponding MSU channel 2 weighting function. This leads to slightly higher brightness temperatures for AMSU for a given incidence angle, especially over land areas, where the surface contribution is larger because of larger emissivity relative to the ocean.

The MSU channel 2 lower-tropospheric (2LT) dataset is based on a weighted difference of MSU views,

$$
\begin{aligned}
T_{\text{2LT-MSU}} &= T_3 + T_4 + T_8 + T_9 \\
&\quad - 0.75(T_1 + T_2 + T_{10} + T_{11}).
\end{aligned}
\tag{3}
$$

This combination of views nearly cancels the stratospheric influence and moves the peak of the temperature weighting function lower in the troposphere (Spencer and Christy 1992). In Fig. 3, we show the 2LT temperature weighting functions for land and ocean surfaces on the same vertical scale as Fig. 2.

Our task now is to find a combination of AMSU measurements that provide the same brightness temperatures as would be found using the combination of MSU measurements presented in Eq. (3). We use a regression method to obtain weights a_{fov} for the AMSU views. The set of equations to be solved are given by

$$
\sum_{\text{fov}} c_{\text{fov}} T_{\text{MSU}}(\text{fov}) = \sum_{\text{fov}} a_{\text{fov}} T_{\text{AMSU}}(\text{fov}),
\tag{4}
$$

where $T_{\text{AMSU}}(\text{fov})$ and $T_{\text{MSU}}(\text{fov})$ are the AMSU and MSU brightness temperatures for each field of view (FOV), respectively. The MSU weights c_{fov} are those given in Eq. (3). Additional equations of the form $k(a_{\text{fov}} - a_{\text{fov}+1}) = 0$ were added to the set of equations before their solution was determined. The effect of these equations is to reduce the effects of noise by introducing a nonparametric smoothness constraint on a as a function of FOV. We solved this equation simultaneously by using monthly zonal averages from *NOAA-14* (MSU) and *NOAA-15* (AMSU) as input data. The zonal averages were calculated over 5° zonal bands, and they were calculated separately for land and ocean scenes and for each FOV. Land areas with surface height averaged over the 2.5° × 2.5° cell that exceed a threshold altitude of 1500 m were excluded from the averages to reduce contamination from surface emission. The land and ocean averages were used to form separate equations to deduce a set of values of a_{fov} that produce

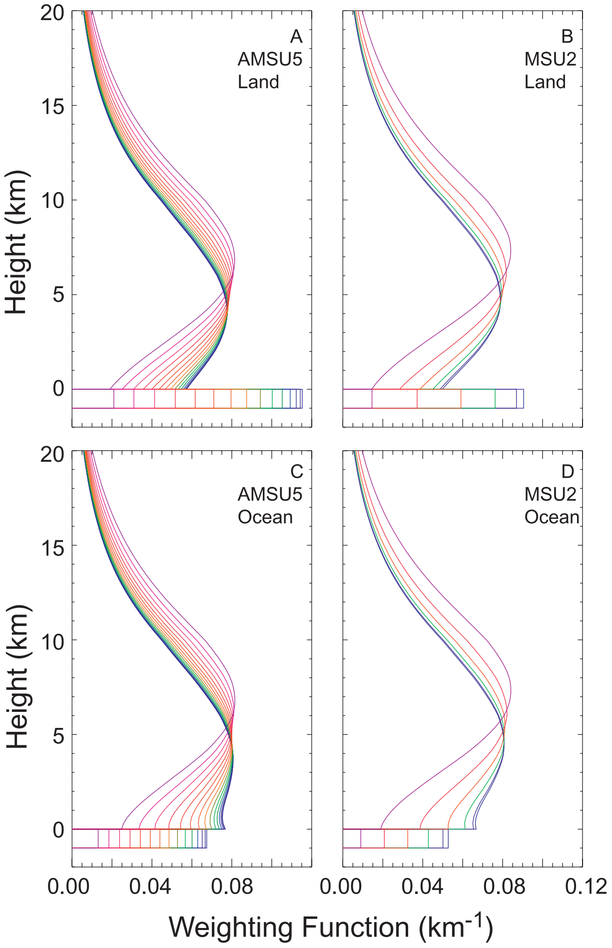

FIG. 2. Temperature weighting functions as a function of altitude for each AMSU and MSU view angle: (a) AMSU channel 5, land; (b) MSU channel 2, land; (c) AMSU channel 5, ocean; and (d) MSU channel 2, ocean. The rectangle at the bottom of (a)–(d) represents the weight resulting from surface emission.

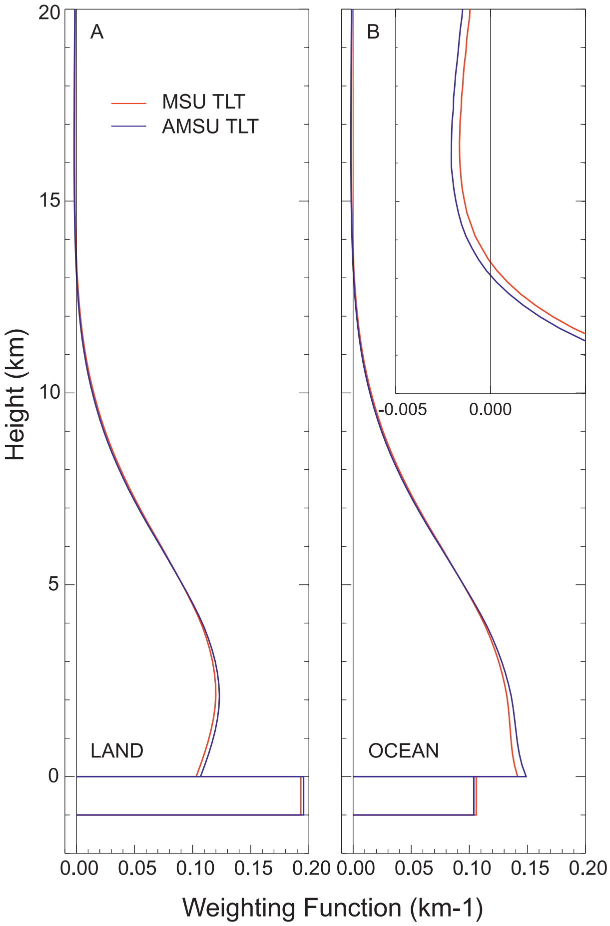

FIG. 3. TLT temperature weighting functions as a function of altitude for MSU and AMSU over (a) land and (b) ocean. The rectangle at the bottom of (a),(b) represents the weight resulting from surface emission. In the inset, we show the two weighting functions on an expanded scale for high altitude.

a good brightness temperature match for both land and ocean scenes independently. Each equation was weighted according to the area of the earth that it represented; that is, for a given zonal band, the land equation was weighted by the land area in that band and the ocean equation was weighted by the ocean area in that band. The values of a_{fov} were constrained to be equal to the corresponding weight on the opposite side of the swath, and the weights for the central 14 views were set to zero so that the derived AMSU product would cover roughly the same part of the swath as the MSU product. (We also performed the calculation with only the central 12 views excluded, which would result in an improved match to the MSU measurement swath; the resulting weight for the innermost included view was so small that we decided to exclude it.) In Table 1, we show the regressed values for the weights of a_{fov}; in Fig. 4, we plot the MSU and AMSU weights as a function of incidence angle. The resulting temperature weighting functions are plotted in Fig. 3 for both ocean and land surfaces, along with the original MSU-derived weighting functions.

The validity of this procedure was evaluated in two ways. First, we studied the residual error between the weighted, zonally, and monthly averaged MSU and AMSU combinations. The standard deviation of the difference between these two combinations is about 0.12K, about 3 times the error we expect because of differences in temporal sampling between the two instruments. Thus, this difference suggests that, although it is impossible to exactly match these weighting functions with a single set of AMSU weights, a reasonably good match can be obtained. Second, Fig. 3 indicates that there is also a good match between the two weighting functions derived using these weights and the *U.S. Standard Atmosphere, 1976*, showing that our combination of views physically matches the temperature weighting of the original MSU 2LT product. Although the differences in weighting functions between the two instruments makes a globally valid, exact solution based solely on view weighting impossible, the weighting procedure developed here minimizes the magnitude of the location-dependent differences between MSU and AMSU measurements. These location-dependent differences will be removed empirically in a later step.

c. *Construction of gridded monthly averages*

All of the adjustment and merging steps discussed in the following sections are performed using monthly averages gridded on a 2.5° × 2.5° longitude and latitude grid. These averages are constructed using the following method: for each half scan (field of view 1–8 or 23–30), a ‘‘lower-tropospheric temperature (TLT) measurement’’ is calculated by applying the weights in Table 1 to the measured temperature for each view and summing. This TLT measurement is then assigned to each 2.5° grid cell that contains the center of a measurement footprint. Then, for each grid cell, all of the TLT measurements for each month are averaged together to form an estimate of the average TLT temperature over the month. Unfortunately, the accuracy of these monthly gridded averages is limited by the differencing procedure. For both MSU and AMSU, the TLT retrieval is a weighted average of near-limb temperatures subtracted from a weighted average of temperatures measured closer to the nadir view. Because the measurements from the various views are not made at the same location on the earth, each TLT measurement is a combination of the desired vertical extrapolation and an unwanted spatial derivative of temperature along the scan direction. In the midlatitudes and tropics, the effect of these spatial derivatives

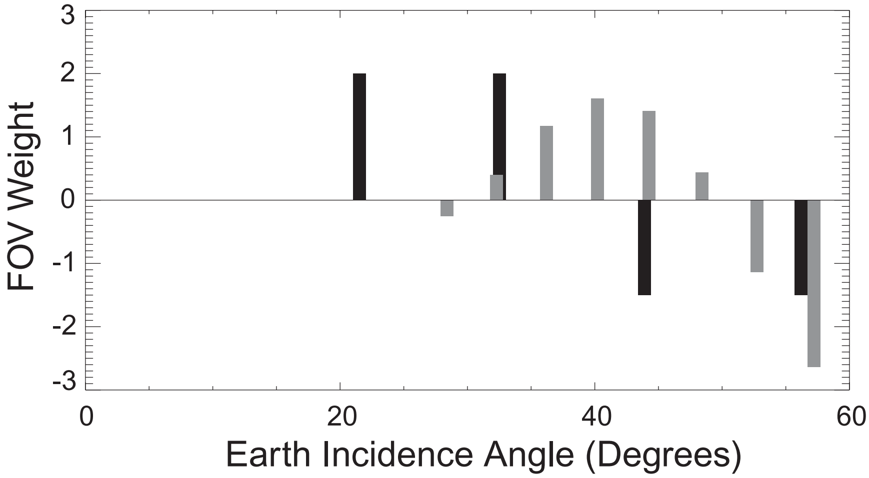

FIG. 4. FOV weights used to calculate TLT plotted as a function of incidence angle for MSU (dark bars) and AMSU (light bars).

on the monthly gridded average is significantly reduced by cancellation of spatial derivatives in different directions, because the monthly average is a combination of right- and left-side views and ascending and descending satellite tracks. Near the poles, cancellation does not occur for the measurements made because the satellite velocity vector is close to being east–west. In this case, the north–south part of the derivative adds instead of canceling. The residual spatial derivative, combined with a large north–south gradient in the temperature, leads to significant errors in the retrieved TLT measurements. These can be reduced if the half scan located equatorward of the satellite is excluded from the average for polar latitudes. For a given latitude, the scanning direction for half scans that come from the equatorward half of their respective scans is closer to being north–south and thus contains a larger gradient-related error. We exclude this half scan completely for latitudes above 60°, and reduce its contribution with a linear latitude-dependent weighting factor for latitudes between 50° and 60°.

d. *Instruments studied*

In this work, we have investigated the use of the data from the nine MSU instruments (ending the use of the *NOAA-14* data after December 2003) and the AMSU instrument on *NOAA-15*. We have determined that AMSU channel 5 on the *NOAA-16* platform suffers from significant unexplained drifts (Mears and Wentz 2009). The premature malfunction of the AMSU instrument on the *NOAA-17* platform yields a time series that is too short to contribute significantly to a long-term dataset. Because two instruments (MSU on *NOAA-14* and AMSU on *NOAA-15*) continued to operate after the *NOAA-17* failure, its use would bring little new long-term information to the data product. We have not yet included data from the *NOAA-18*, *Meteorological Operation-A* (*MetOP-A*), or *Aqua* satellites in our analysis.

3. Merging procedure

Our merging procedure for TLT closely follows the methods we used for the simpler, nonextrapolated MSU–AMSU datasets, which are described in detail in an earlier paper (Mears and Wentz 2009). Here, we focus extra attention on those details that are unique or important to the TLT dataset.

a. *Premerge adjustments*

1) INCIDENCE ANGLE ADJUSTMENTS

Although the viewing angle of each observation ideally depends only on the view number, the earth incidence angle also depends on the height of the satellite

TABLE 1. Regressed values for the weights a_{fov}.

a_{15}, a_{16}	0.00
a_{14}, a_{17}	0.00
a_{13}, a_{18}	0.00
a_{12}, a_{29}	0.00
a_{11}, a_{20}	0.00
a_{10}, a_{21}	0.00
a_9, a_{22}	0.00
a_8, a_{23}	−0.25
a_7, a_{24}	0.40
a_6, a_{25}	1.17
a_5, a_{26}	1.61
a_4, a_{27}	1.41
a_3, a_{28}	0.44
a_2, a_{29}	−1.14
a_1, a_{30}	−2.64

above the earth's surface and the local curvature of the earth. Both these factors change during a single orbit of the satellite due to both the oblate shape of the earth and the elliptical nature of the satellite's orbit. In addition, the average height of the satellite tends to decay over time because of atmospheric drag on the satellite. These changes in incidence angle substantially change the pathlength of the near-limb views through the atmosphere, and thus can affect the weighting function and the measured brightness temperature. This is particularly important for TLT because weighted differences are used to retrieve the lower-tropospheric temperature. To minimize this effect, each observation is adjusted to correspond to a nominal incidence angle corresponding to its field of view. This procedure implicitly removes the effects of the decay in orbital height (Wentz and Schabel 1998). A first-order adjustment is made using simulated brightness temperatures calculated from an atmospheric profile climatology based on the NCEP reanalysis (Kalnay et al. 1996; Mears et al. 2003). This part of the adjustment is performed by the middle two terms in Eq. (5). For MSU channel 2, we found that we had to include an additional term that was well-modeled as a time-dependent instrument roll (Mears et al. 2003) to remove a persistent bias between measurements on opposite sides of the swath. For AMSU channel 5, we found that after performing the model-based adjustment, an additional empirical correction $T_0(\text{fov})$ for each field of view (not well described by an instrument roll) was needed to remove residual cross-track biases (Mears and Wentz 2009).

$$T_{\text{Adj}} = T_{\text{AMSU}}(\text{fov}) + T_{\text{Mod}}(\theta_{\text{nom}}) - T_{\text{Mod}}(\text{fov}) + T_0(\text{fov}). \tag{5}$$

We define the empirical correction $T_0(\text{fov})$ to be independent of location on the earth and time of year. Because this adjustment is independent of time, it does not directly affect long-term changes in the resulting dataset. It does serve to slightly reduce the variability in intersatellite differences, and thus may improve the accuracy of our merging procedure.

2) DIURNAL ADJUSTMENT

Drifts in local measurement time can alias the local diurnal cycle into the long-term time series if corrections are not applied. For AMSU measurements, we use the same technique we used for MSU, which is described in a previous paper (Mears et al. 2003). Using 5 yr of hourly output from the CCM3 climate model (Kiehl et al. 1996), we created a diurnal climatology for the MSU2 and AMSU5 frequencies as a function of incidence angle (Mears et al. 2002; Mears and Wentz 2009). This diurnal climatology is used to adjust each measurement so that it corresponds to local noon. For long-lived satellites that suffer substantial drifts in measurement time, such as *NOAA-11*, *NOAA-14*, and *NOAA-15*, this adjustment can be quite important, and uncertainty in the adjustment can be a major source of uncertainty in the final results.

b. Determination of target factors

Differences between globally averaged measurements made at the same time by different MSU and AMSU instruments can have a component that is strongly correlated with the temperature of the warm calibration target of one or both satellites, suggesting that there may be a calibration error that is dependent on calibration target temperature. This effect was first noticed by Christy and coworkers (Christy et al. 2000). Possible causes for these calibration errors include residual nonlinearity in the radiometer response that was not adequately measured during ground calibration or an error in the specification of the effective brightness temperature of the calibration sources. Both these error sources imply an additional error that is dependent on the scene temperature (Mears and Wentz 2009). Our empirical error model that includes both target temperature– and scene temperature–dependent errors is given by

$$T_{\text{MEAS},i} = T_0 + A_i + \alpha_i T_{\text{TARGET},i} + \beta_i T_{\text{SCENE}} + \varepsilon_i, \tag{6}$$

where T_0 is the true brightness temperature, A_i is the temperature offset for the ith instrument, α_i is a small multiplicative "target factor" describing the correlation between the measurement error and the temperature of the hot calibration target, and $T_{\text{TARGET},i}$ is the target temperature anomaly for the ith satellite. The "scene factor" β_i describes the correlation between the measurement error and the scene temperature T_{SCENE}; ε_i is an error term that contains additional uncorrelated zero-mean errors resulting from instrumental noise and sampling effects. In our previous work, we found that the target factors α_i are necessary to accurately match the overlapping observations for the MSU instruments, which confirms the earlier results of Christy et al. (2000), though we sometimes find different numerical values for α_i.

We determine the target factors by using an analysis of globally averaged (50°S–50°N) TLT observations adjusted for satellite height and measurement time effects. As was the case for the simple nonextrapolated MSU–AMSU datasets, we choose to perform this calculation separately for the MSU and AMSU sets of satellites (Mears and Wentz 2009) because of small seasonal differences between the MSU and AMSU data.

TABLE 2. Merging parameters for MSU TLT.

Satellite	Target factor α (simple regression)	Target factor α (with magnitude reduction equations; used in this work)	Target temperature factor α (Mears and Wentz 2005)	Target temperature factor α (Christy et al. 2000)	Scene temperature factor β
TIROS-N	−0.0267	−0.0224	−0.0089	0.0	0.0076
NOAA-6	0.0003	0.0018	0.0001	0.002	0.0079
NOAA-7	0.0072	0.0096	0.0110	0.018	0.0061
NOAA-8	0.0378	0.0381	0.0307	0.036	−0.0059
NOAA-9	0.0691	0.0486	0.0383	0.095	−0.0055
NOAA-10	0.0087	0.0086	0.0059	0.0	−0.0064
NOAA-11	0.0320	0.0319	0.0280	0.035	−0.0053
NOAA-12	0.0061	0.0061	0.0060	0.007	0.0006
NOAA-14	0.0248	0.0239	0.0248	0.015	0.0009

For MSU, we closely follow the method described in Mears and Wentz (2009). For each month when two or more satellites are observing simultaneously, we form an equation by taking the difference between versions of Eq. (6) for each satellite pair,

$$T_{\mathrm{MEAS},i} - T_{\mathrm{MEAS},j} = A_i - A_j + \alpha_i T_{\mathrm{TARGET},i} - \alpha_j T_{\mathrm{TARGET},j}, \tag{7}$$

thus eliminating the true brightness temperature. For now, we ignore the scene temperature term, which will be discussed in section 4d. For MSU TLT, this results in a system of equations with 182 equations in 17 unknowns (8 offsets and 9 target factors; one offset, $A_{NOAA\text{-}10}$, is arbitrarily set to zero to prevent a singular system of equations). The system is then solved using singular value decomposition to find the target factors. The offsets values are discarded. The final values for the offsets will be determined as a function of latitude in the next step. The values of the target factors determined by this calculation are tabulated in Table 2.

The deduced value for the *NOAA-9* target factor (0.0691) is significantly larger than the corresponding value we found for MSU TMT (0.0362). The TMT target factors were calculated using a simple average of near-nadir views, which is in contrast to the nadir-limb differencing used to construct the TLT temperatures. The differencing procedure amplifies any noise present so that we expect the noise in the TLT global averages to be larger than the TMT averages (Mears and Wentz 2005). Under the assumption of uncorrelated noise in each FOV, the noise in TLT averages is given by the quadrature sum of the noise in each FOV weighted by the absolute value of the weight for each FOV; for MSU, it is $5\sqrt{5/4} \cong 5.567$ times larger than the noise in MSU TMT. Furthermore, investigation of the covariance matrix for the regression reveals that the *NOAA-9* target factor is poorly determined because of the short overlap period with other satellites and the relatively small seasonal-scale fluctuations in the *NOAA-9* target temperature. Taken together, these facts lead us to suspect that the fitted value for the *NOAA-9* target factors is too large because of overfitting of noise. Examination of the regression results suggests that there are solutions that are nearly as good as the best fit but with smaller values of the *NOAA-9* target factor. To reduce the values of the target factors, we add nine ad hoc equations to the regression of the form

$$CT_{\mathrm{TARGET},i} = 0.0. \tag{8}$$

In our overdetermined system, these equations have the effect of "pulling" the target factors toward zero, with the amount of the pull determined by the constant C. If a given target factor is well determined by the other equations in the regression, the effect of these additional equations will be small. On the other hand, if a target factor is poorly determined (and thus subject to overfitting) its absolute value will be reduced significantly. When C is set to 1.0, the absolute values of the target factors for *TIROS-N* and *NOAA-9* are reduced substantially, with little effect on the target factors for the other instruments. The values for the target factors with C set to 1.0 are shown in the third column of Table 2. We choose to use these "magnitude reduced" target factors to adjust the TLT data because the *NOAA-9* target factor (0.0486) is closer to the value found for TMT. We note that this is a subjective decision that has the effect of increasing the final global trend by about 10%. For comparison purposes, we also show the TLT target factors we used in our earlier work (Mears and Wentz 2005) and used by Christy et al. (2000). Our current *NOAA-9* target factor is larger than its earlier value but still much smaller than the value found by Christy et al. (2000). This difference is an important contributor to the differences between our respective datasets and an important source of "structural" uncertainty, the

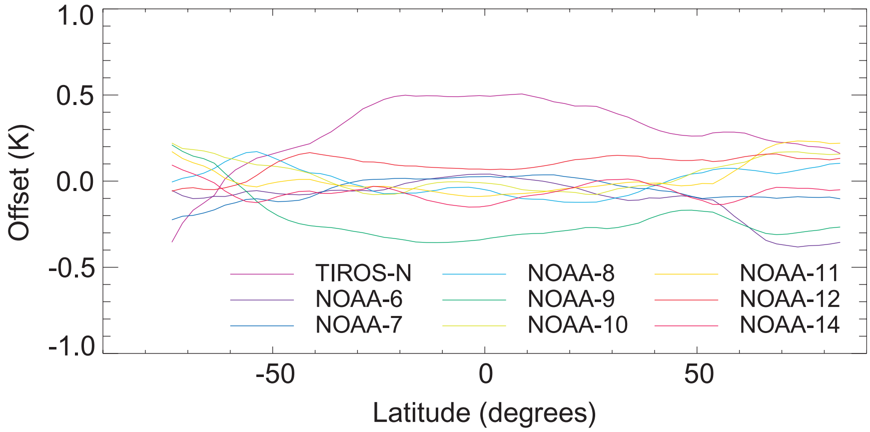

FIG. 5. Time-invariant temperature offsets applied to measurements from each MSU satellite as a function of latitude.

uncertainty that arises because of the choice of methodology (Thorne et al. 2005a).

As noted above, we have found that channel 5 for *NOAA-16* is contaminated by an unexplained drift in measured temperature. This complicates the determination of the target factors for *NOAA-15*. Following Mears and Wentz (2009), we use detrended versions of the measured temperature and the target temperatures to find the value of the *NOAA-15* TLT target factor to be 0.004, a value so small that it is unimportant to the final results.

c. *Latitude-dependent offsets*

Since developing the MSU-only version of our dataset (Mears and Wentz 2005), we have determined that zonally averaged intersatellite differences can be substantial when the constant terms (A_i) are held constant as a function of latitude. This led us to extend our empirical model so that the values of A_i are allowed to smoothly vary with latitude, which is similar to the approach used by Christy et al. (2000). To determine the latitude dependence of the offsets, we simultaneously solve a system of equations given by

$$T_{\mathrm{MEAS},i,k} - T_{\mathrm{MEAS},j,k} = A_{i,k} - A_{j,k} + \alpha_i T_{\mathrm{TARGET},i,k} - \alpha_j T_{\mathrm{TARGET},j,k}. \tag{9}$$

This equation is a version of Eq. (6) generalized so that each equation describes the difference between measurements made by the ith and jth satellites for the kth zonal band, where the values of $A_{i,k}$ are allowed to vary with latitude. We performed the calculation for 2.5° wide bands and formed an equation for each latitude band and month where two or more satellites were observing simultaneously. The target factors α_i were set to the values found in the previous step. Singular value decomposition was used to determine the solution to the system of equations. The use of singular value decomposition finds the minimal variance solution for the offsets so that we change the measured temperatures by the least possible amount. To reduce the effects of noise on the retrieved offset values, we smooth the offsets in the north–south direction using a ''boxcar'' smooth with a width of 12.5°. Figure 5 shows the smoothed offsets as a function of latitude for each of the nine MSU satellites used in this study. The differences between the MSU and AMSU measurements are too complex to be described by latitude-dependent offsets and are addressed separately in section 3e.

d. *Scene temperature–dependent errors*

When we apply the target factors and offset determined in the previous steps to the data and evaluate the intersatellite differences, we find significant seasonal-scale fluctuations near the poles, where the seasonal cycle is large, but not near the equator, where the seasonal cycle is small. This suggests that part of the remaining differences is caused by a scene temperature–related calibration error. To attempt to correct for this error, we again take the difference between versions of Eq. (6) for each month that two or more satellites are observing simultaneously. Substituting the values already determined for $A_{i,j}$ and the α_i into

$$T_{\mathrm{ADJ},i,k} = T_{\mathrm{MEAS},i} - A_{i,k} - \alpha_i T_{\mathrm{TARGET},i,k} \tag{10}$$

and keeping the T_{SCENE} dependence from Eq. (3), we obtain a system of equations given by

$$\begin{aligned} T_{\mathrm{ADJ},i,k} - T_{\mathrm{ADJ},j,k} &= \beta_i T_{\mathrm{SCENE},i,k} - \beta_j T_{\mathrm{SCENE},j,k} \\ &= (\beta_i - \beta_j) T_{\mathrm{SCENE},k} \end{aligned} \tag{11}$$

for each zonal band. We can replace $T_{\mathrm{SCENE},i,k}$ and $T_{\mathrm{SCENE},j,k}$ with $T_{\mathrm{SCENE},k}$ because the scene temperature is a property of the earth and thus independent of the satellite index. Here, T_{SCENE} is closely approximated by the measured antenna temperatures. We use an average value for T_{SCENE} found by averaging the results from all satellites over 1979–98 to form a TLT climatology that depends on latitude and month. These values are then used in the system of equations described by Eq. (11) to deduce the values for β. Because β_i only appears in the equations as the difference between the values of β for different satellites, its average value is arbitrary. We use singular value decomposition to choose the minimum-variance solution for β_i. We report the values of β for each satellite in Table 2.

To display the effects of these various intercalibration steps, we show in Fig. 6 the color-coded time–latitude plots of the intersatellite differences at different stages in the intercalibration process for an example pair of satellites, *NOAA-11* and *NOAA-12*. Figure 6 shows that the reduction in intersatellite differences for these two satellites is quite small for the scene temperature step. We retain this step in this case for the sake of consistency with other satellite pairs and our other MSU-derived datasets. Because the scene temperature factors are fairly small, they have only a small effect in the tropics and lower midlatitudes, where the seasonal cycle is much smaller than near the poles. In the bottom panel of Fig. 6, we show time series of near-global averages (50°S–50°N) of the monthly differences between *NOAA-11* and *NOAA-12* for both the raw antenna temperatures and after all adjustments were applied. A comparison of this plot to the corresponding plots for the near-nadir views (Mears and Wentz 2009, their Fig. 6) shows that additional noise is present in the fully adjusted differences for TLT, as we expect because of the noise amplification that occurs during the calculation of the weighted FOV differences.

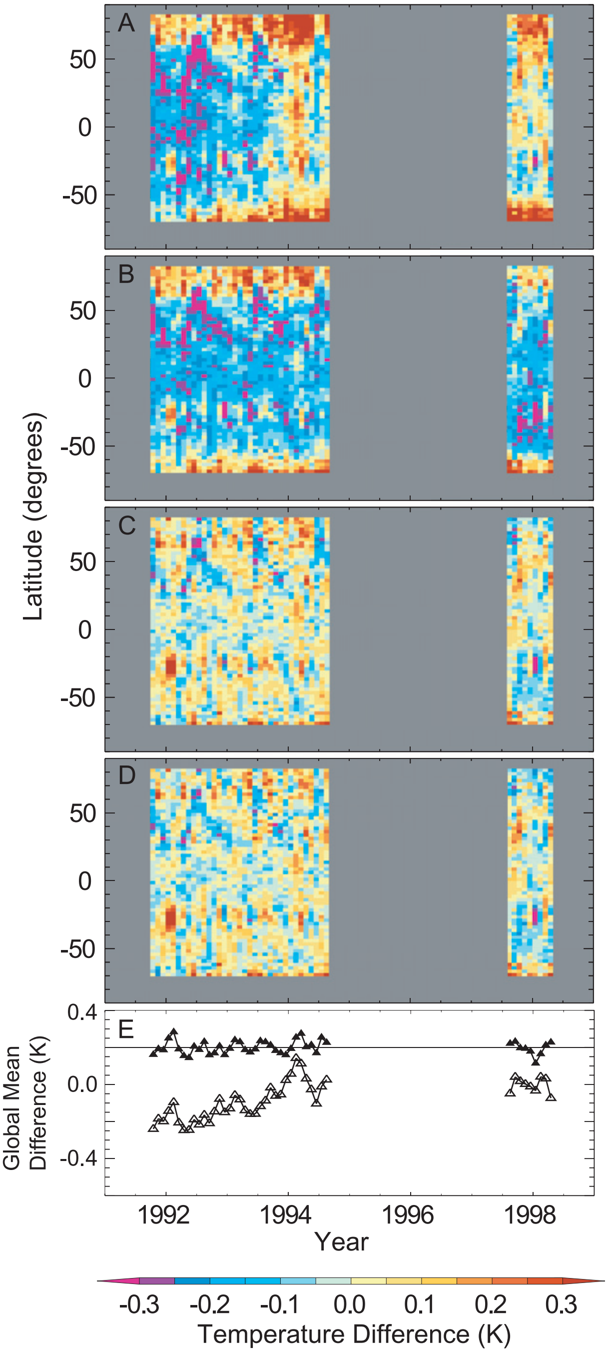

FIG. 6. Differences (*NOAA-11* − *NOAA-12*) between TLT measurements as a function of latitude and time. (a) Uncalibrated data with only the diurnal and incidence angle adjustments made. Note the large trend in the difference, particularly during 1993–95. (b) Differences after the target temperature adjustments are applied. The large trend has been removed, as well as much of the quasi-periodic differences. (c) Differences after the latitude-dependent offsets are applied, which remove the large overall differences in the low latitudes. (d) Differences after the scene temperature adjustments are applied. For this satellite pair, the scene temperature adjustments make little difference.

e. *Location- and month-dependent offsets between MSU TLT and AMSU TLT*

The AMSU FOV weights determined in section 2b match the results for MSU TLT and AMSU TLT as best as possible for average atmospheric and surface conditions. However, the match is not perfect and small differences remain. These differences are caused by a combination of 1) small differences in the temperature weighting function coupled with local values of the vertical structure of the atmosphere and of the emissivity and temperature of the surface and 2) different amounts of spatial smoothing and spatial derivative inadvertently accomplished by the FOV weighting for the

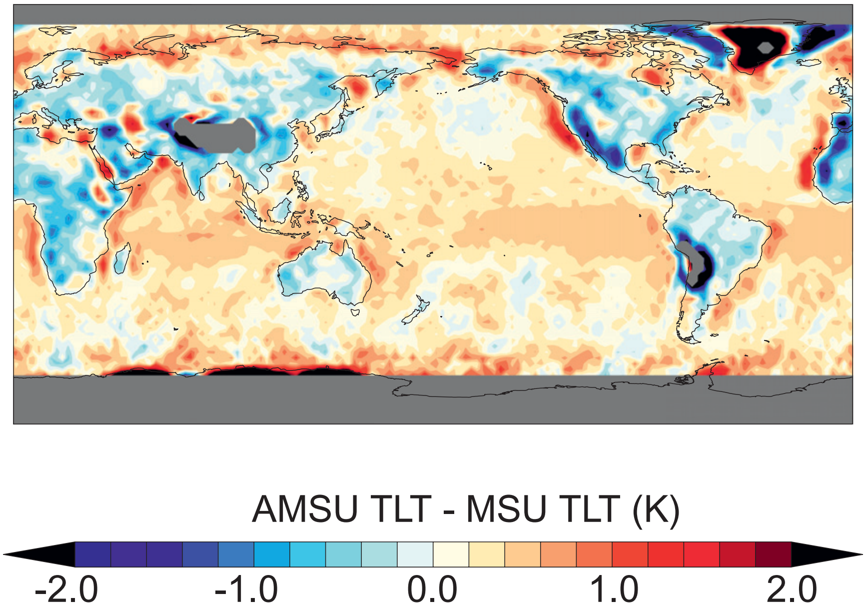

FIG. 7. Map of mean *NOAA-15* (AMSU) and *NOAA-14* (MSU) TLT differences for the month of June. The differences are averaged over 1999–2003.

two satellite types. To minimize the effect of these errors on the MSU–AMSU merging procedure, we need to find the average difference between MSU and AMSU TLT data and use this average to adjust the AMSU data so that they correspond to the MSU data before merging the two datasets together. We will perform this adjustment as a function of earth location and time of year to remove the most important part of these errors.

In Fig. 7, we plot the mean difference [*NOAA-14* (MSU) minus *NOAA-15* (AMSU)] in TLT brightness temperature for the month of June. Data from 1999 to 2003 are included in the average. The most obvious differences occur near the edges of continents—these are due to the different spatial smoothing and spatial derivative caused by using the weighting average of different FOVs. Similar maps are computed for all other months, and a two-harmonic seasonal fit is calculated at each point. These differences are used to adjust the AMSU data so that they match the MSU data. In practice, we use maps of the parameters of harmonic fits (i.e., constant offsets plus the amplitudes and phases of the seasonal cycle) to the seasonal cycle at each point to generate an adjustment for the AMSU data that is dependent on location and month.

f. Merging data from different satellites

After all the adjustments are applied to the MSU data, we evaluate the intersatellite differences for any remaining problems. As was the case in the simple, nonextrapolated case, we found that several satellites had averages for several months that appeared to be anomalously high or low (Mears and Wentz 2009). These typically occurred near the beginning or end of each satellite's lifetime and were often associated with months where several days of data were missing (causing sampling errors) or with times when data quality was noted to have deteriorated by the satellite operations team at NOAA (Goodrum et al. 2000; Kidwell 1998). In other cases, no cause could be identified. These spurious months, which are listed in Table 3, were excluded from further processing. The data from different MSU satellites were then combined by using simple averaging when data from more than one satellite were present. For AMSU, only one satellite is currently used; therefore, no merging is necessary to produce an AMSU-only dataset. Data from the two satellite types are then combined by again using simple averaging when data from both satellite types are present. A record of which satellites are used for each month is kept and propagated through subsequent steps to become part of the final data product.

TABLE 3. The months that several satellites were manually excluded from processing.

Satellite	Months excluded
TIROS-N	March 1980
NOAA-6	April 1983
NOAA-11	September–December 1994
NOAA-12	May–September 1991

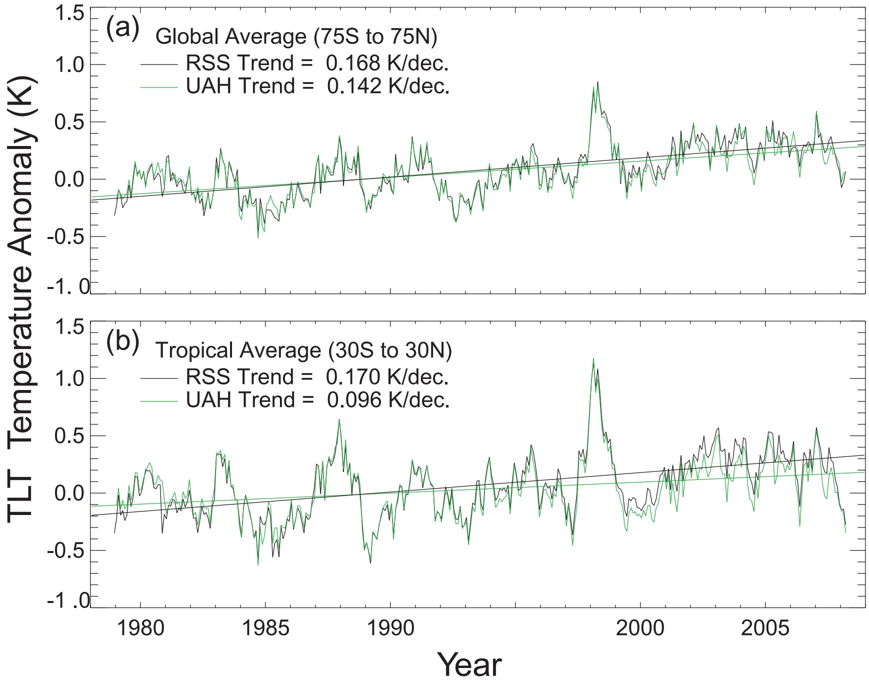

FIG. 8. (a) Global (75°S–75°N) and (b) tropical (30°S–30°N) TLT anomaly time series. The anomalies are calculated relative to a 1979–98 base period, and the trends are calculated over 1979–2007.

4. Results

Our resulting dataset is freely available to all in a number of formats via the Internet (available online at http://www.remss.com/msu/). Here, we provide a short summary of some of the important features of the dataset.

In Fig. 8, we plot the global (75°S–75°N) and tropical (30°S–30°N) TLT temperature anomalies, calculated relative to a 1979–98 average. Both the tropical and global time series show significant warming and are dominated by strong warming during the 1997/98 El Niño event. Other El Niño and La Niña events can also be seen, including the strong La Niña during the most recent (2007/08) winter.

In Fig. 9, we show the decadal trends as a function of latitude. We find that the strongest warming occurs in the northern polar regions, with trends exceeding 0.3 K decade^{-1} north of 60°N. In the Southern Hemisphere, we find very little high-latitude warming, with no significant warming south of 50°S.

In Fig. 10a, we show a color-coded map of decadal trends over 1979–2007. Again, northern high-latitude warming dominates, with strong warming over most parts of the Arctic. Strong warming is also present in east-central Asia. Cooling is occurring over much of the southern oceans, with strong cooling occurring south of New Zealand.

5. Comparison with other estimates of tropospheric temperature change

In this section, we compare our dataset with other observations of lower-tropospheric temperature in recent decades. We choose to compare to the UAH version of the MSU–AMSU TLT dataset (Christy et al. 2000; Christy et al. 2003), as well as four datasets based on homogenized radiosonde measurements. Other sources of tropospheric temperature measurements—for example, radio occultation measurements made with global positioning system satellites (e.g., Kursinski et al. 1997)—are not available over a long-enough time period to make useful comparisons of changes over multiple decades.

a. *Comparison with the UAH TLT dataset*

The UAH MSU–AMSU TLT dataset is made using the same raw measurements as our dataset, so any differences between the two datasets are the result of differences in methods used to construct the long-term climate data record. In Fig. 8, we plot the global and tropical anomaly time series for each dataset. On short time scales, the two datasets are very similar, as might be expected because they both originate from the same satellite measurements. Over longer periods, some small differences become apparent, with the RSS dataset showing more warming for both the global and tropical averages.

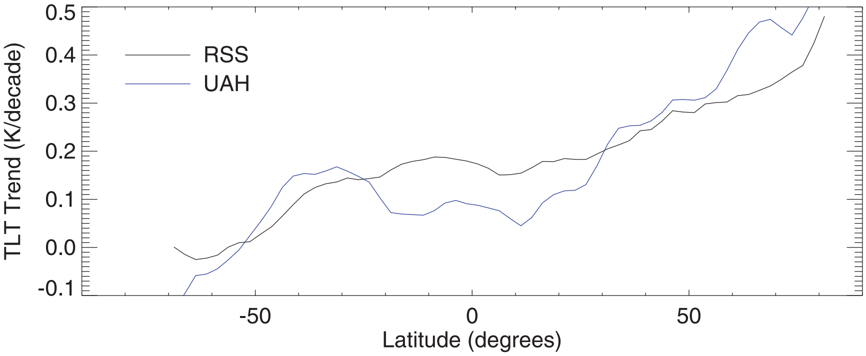

FIG. 9. Decadal trends (1979–2007) in TLT as a function of latitude for RSS and UAH V5.2.

The cause of these differences is likely to be a combination of several factors, including different quality-control algorithms, different values for the target factors (see Table 2), and the different methods used to perform the diurnal adjustment. In particular, the different target factor for *NOAA-9* causes the differences in the 1985–87 period, whereas differences in the diurnal adjustment and the *NOAA-11* target factor combine to produce the changes between 1991 and 1996. For both global and tropical trends, the differences between the two datasets are smaller than the estimated 2σ error in our earlier MSU-only TLT trends (Mears and Wentz 2005). The trend error estimates in Mears and Wentz (2005) were obtained by estimating the uncertainty in the merging parameters and the diurnal adjustment. Although these earlier estimates do not yet include the effects of including AMSU data in our procedure, they can serve as a first guess of the magnitude of the error. The trend differences between the RSS and UAH results are due to differences in merging procedure and primarily occur at time scales longer than one year. For this reason, the uncertainty in trend difference that can be inferred from the standard deviation of the difference time series is much smaller than the observed difference in trends.

In Fig. 9, we plot the 1979–2007 TLT trends as a function of latitude for both datasets. Each dataset shows the same general pattern, with little warming (or even cooling) south of 50°S and the largest warming in the Northern Hemisphere polar regions. The RSS data show significantly more warming in the tropics than the UAH dataset. Because the effects of the target factors are nearly constant with location, this difference is likely to be due to differences in the diurnal adjustments and the effect of these differences on the latitude-dependent offsets.

In Fig. 10, we show color-coded maps of 1979–2007 trends for both datasets and their difference. The overall patterns are very similar, though the UAH trends are noticeably smoother in the east–west directions because of their spatial smoothing procedure (Christy et al. 2000, 2003). The difference map suggests that much of the differences between these datasets are a function of latitude, again pointing to differences in the diurnal adjustment as the primary cause.

b. *Comparison with homogenized radiosonde datasets*

It is well established that temperature measurements made by radiosondes contain numerous inhomogeneities resulting from changes in instrumentation and observing practices over time. Before radiosonde measurements can be used to describe long-term changes, these inhomogeneities need to be characterized and removed to the largest possible extent. A number of groups have produced homogenized radiosonde datasets. For comparison with our satellite measurements of TLT, we chose four of the most recent homogenized datasets. These datasets are either available as gridded TLT measurements or contain enough information so that it is possible for us to construct a gridded TLT dataset. These datasets were constructed using automated methods to find and estimate the size of ''breakpoints'' in each radiosonde's time series, which are then used to create adjusted versions of the radiosonde data with the effects of the detected breakpoints removed. We list each radiosonde dataset below.

1) HADAT

The Hadley Centre Atmospheric Radiosonde Temperature Product (HadAT) is constructed by analyzing the difference between the monthly time series from a given radiosonde and a composite of neighboring radiosondes (Thorne et al. 2005b). The earlier human-analyzed Lanzante–Klein–Seidel (LKS; Lanzante et al. 2003) dataset is used as a starting point, and LKS is assumed to contain no large inhomogeneities.

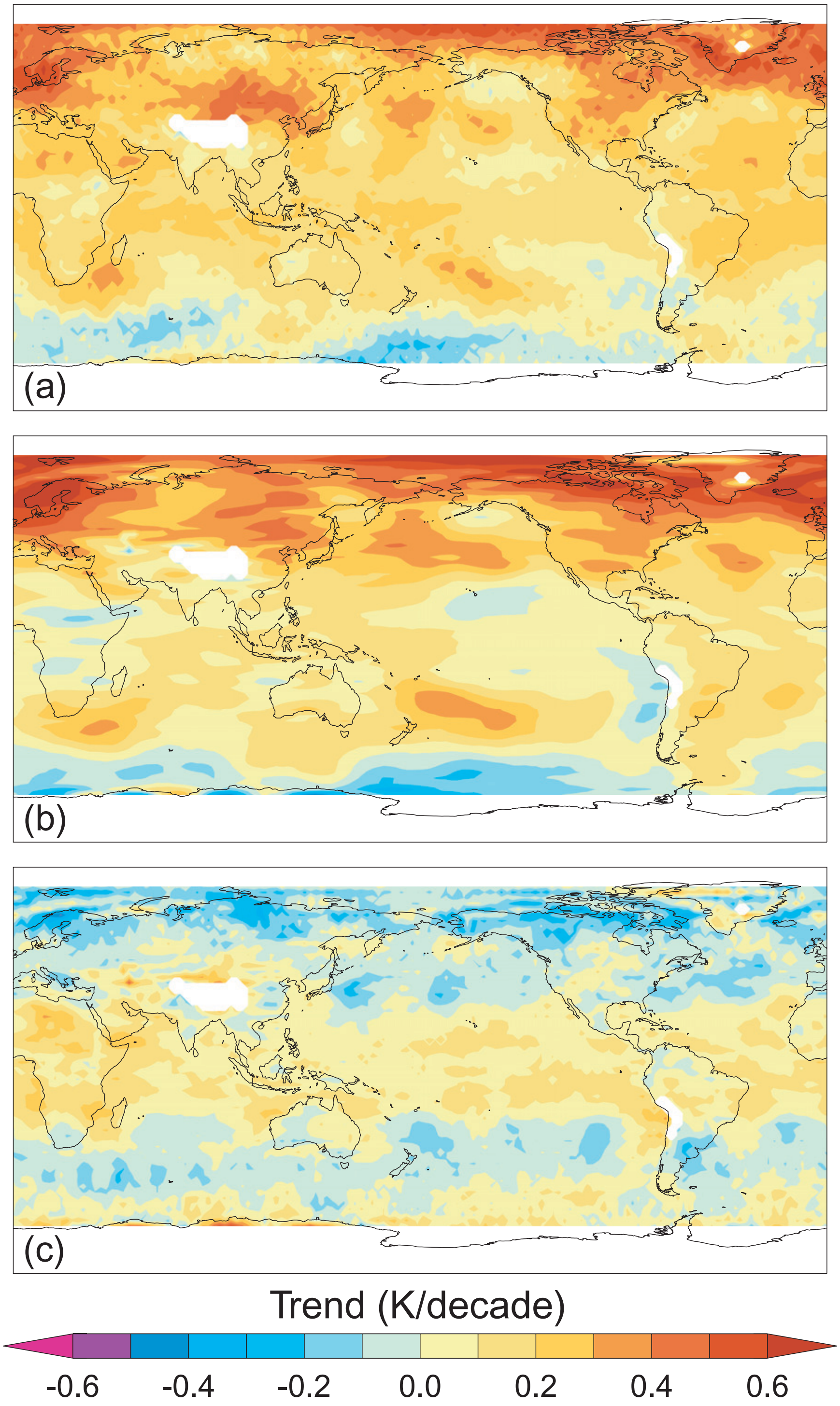

FIG. 10. Maps of trends in TLT for 1979–2007 for (a) RSS V3.2 (this work), (b) UAH V5.2, and (c) RSS and UAH V5.2.

2) RAOBCORE

The Radiosonde Observation Correction using Reanalysis (RAOBCORE; Haimberger 2007; Lanzante et al. 2003) dataset is constructed at the University of Vienna by evaluating the difference between individual (daily at 0000 or 1200 UTC) radiosonde observations and background forecast fields calculated during the construction of the

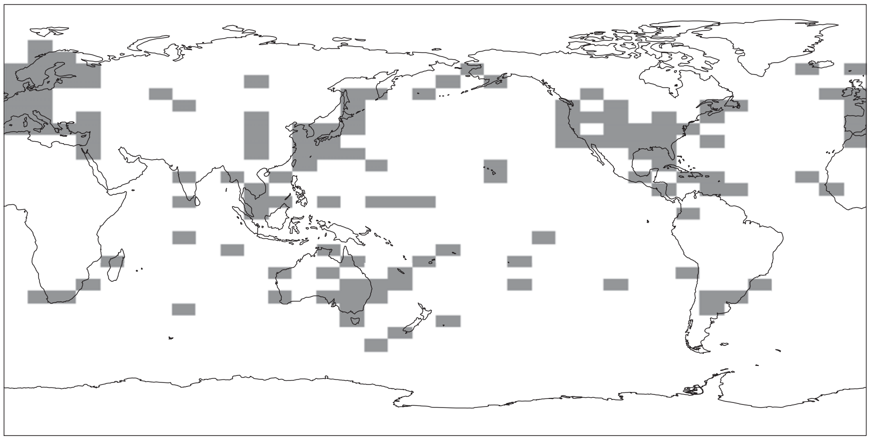

FIG. 11. Sampling pattern for the HadAT dataset for January 2003. Gray boxes are valid data, and white regions are missing data.

40-yr European Centre for Medium-Range Weather Forecasts (ECMWF) Re-Analysis (ERA-40). Because ERA-40 uses measurements from MSU and AMSU during its construction, RAOBCORE cannot be considered to be completely independent of the satellite measurements. RAOBCORE uses the background fields to both detect and estimate the size of breakpoints in the satellite record.

3) RICH

In contrast, the Radiosonde Innovation Composite Homogenization (RICH; Haimberger et al. 2008) dataset uses the breakpoints identified by the RAOBCORE analysis but estimates the size of any jumps using a composite of neighboring stations. Thus, the amount of adjustment performed for each breakpoint is independent of ERA-40 and satellite measurements.

4) IUK

The radiosonde Iterative Universal Kriging (IUK; Sherwood et al. 2008) dataset is constructed at Yale University using an analysis method that simultaneously evaluates long-term variability and observing biases using an iterative kriging approach (Sherwood 2007). This method also depends on the analysis of neighboring stations, but it is designed to be robust with respect to errors resulting from inhomogeneities in these neighbors.

To compare the results of these datasets with satellite-derived TLT datasets, TLT-equivalent versions of the radiosonde datasets need to be calculated. This is done by calculating weighted vertical averages of the discrete-level radiosonde data using weights calculated so that the effective weighting function of the resulting average closely matches the TLT weighting functions. For HadAT and RAOBCORE, this is already performed by the originating institutions; both of these datasets are available as gridded TLT-equivalent temperatures. RICH data are available as gridded products at 12 pressure levels from 850 to 30 hPa. Using these temperatures along with surface temperatures from HadCRUT3, we calculated equivalent TLT temperatures for RICH.

The IUK dataset is available as adjusted monthly profiles at each radiosonde location. We binned each monthly measurement into a 10° × 10° grid using ‘‘bucket’’ sampling and then calculated TLT-equivalent temperatures using Hadley Centre Climatic Research Unit, version 3 (HadCRUT3) surface temperatures.

We compared the satellite and homogenized radiosonde temperature anomalies by comparing time series and trends of large spatial-scale averages. Large spatial-scale averages are more useful because of the significant uncertainties in the measurements from isolated radiosondes and in single satellite grid points. Over larger spatial scales, these uncertainties are reduced by the averaging procedure. We choose to focus on global averages (75°S–75°N), the southern extratropics (SXT; 75°–30°S), the tropics (30°S–30°N), and the northern extratropics (NXT; 30°–75°N). In all regions, but especially the tropics and the SXT, radiosonde spatial coverage is far from complete. Figure 11 shows a typical radiosonde sampling pattern. Comparing trends of simple area-weighted (AW) global averages of radiosonde data with the area-weighted means of the spatially complete satellite data will lead to substantial discrepancies because of the large unsampled areas in the SXT, where the trends are much lower than in the well-sampled NXT. We tried two approaches to account for these sampling differences. In our first approach, we changed the averaging procedure for the radiosonde data by calculating means in 5° latitude bands and then calculating a global mean from a cosine (latitude)-weighted average of the zonal means. We refer to this mean as a zonal-global

TABLE 4. Standard deviations of detrended differences.

	AW satellite − AW radiosonde	AW satellite − ZG radiosonde	SRL satellite − AW radiosonde
RSS–HadAT	0.172	0.139	0.066
UAH–HadAT	0.176	0.135	0.082
RSS–RAOBCORE	0.128	0.083	0.074
UAH–RAOBCORE	0.133	0.064	0.085
RSS–RICH	0.124	0.097	0.066
UAH–RICH	0.130	0.082	0.073
RSS–IUK	0.104	0.103	0.067
UAH–IUK	0.108	0.096	0.074

(ZG) mean. This is intended to modify the radiosonde means so that they more closely resemble the spatially complete satellite mean. This approach is similar to those commonly used to generate global trends from the radiosonde data (e.g., Thorne et al. 2005b). In our second approach, we sampled the satellite data using the actual radiosonde sampling for each month and then computed an area-weighted average. This approach is intended to modify the satellite means so that they closely match the area-weighted radiosonde means and they automatically take into account the presence or absence of a radiosonde measurement for a given location and month. We refer to the sampled satellite means as ''sampled at radiosonde locations'' (SRL).

To compare the success of each method in matching the radiosonde time series to the satellite time series, we compare standard deviations of two sets of difference time series: AW satellite–ZG radiosonde and SRL satellite–AW radiosonde. Table 4 shows the standard deviation for each satellite–radiosonde dataset pair for global (75°S–75°N) averages. The lowest values are for time series constructed using SRL satellite–AW radiosonde means. Difference time series constructed from AW satellite–ZG radiosonde means often show considerably larger standard deviations, suggesting that the global averages constructed using the ZG averaging procedure still contain significant sampling errors. We conclude that the SRL method does a better job of accounting for sampling errors and choose to use this method when comparing decadal trends in satellite and radiosonde data. Note that although the SRL satellite and AW radiosonde means appear to be the best choice for comparing the two types of data, they are not good representations of the actual global means because they both contain potentially large (but similar) sampling errors.

In Fig. 12, we show global time series for an example radiosonde dataset (RICH), and AW and SRL satellite time series. The SRL procedure improves both the agreement between long-term trends and the agreement in short-term fluctuations. Obvious examples of the improvement in short-term fluctuations can be seen in 1985, 1989, and 1999–2000.

In Table 5 and Fig. 13, we present the 1979–2006 trends for each dataset and for the global, SXT, tropical, and NXT regions. For satellite trends, we present both

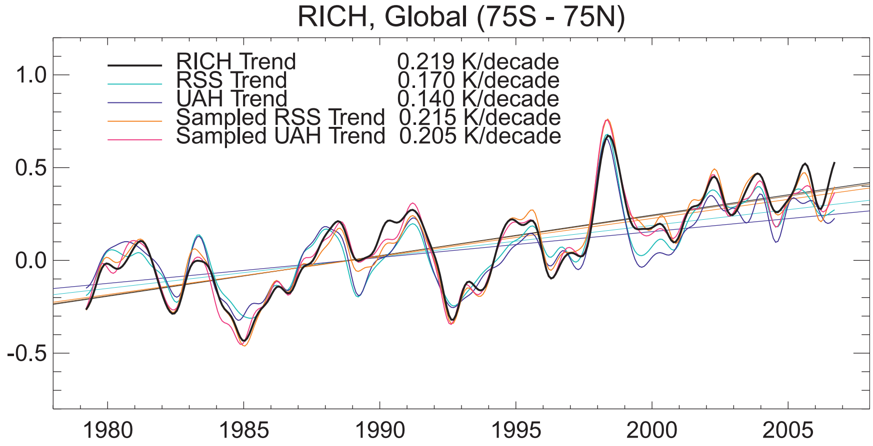

FIG. 12. Example radiosonde (RICH) and satellite TLT anomaly time series for 1979–2006. All time series have been smoothed using a filter with a cut-off period of 6 months. The sampled satellite time series and trends are calculated using an AW average of grid points with valid RICH data for each month.

TABLE 5. Satellite and radiosonde trend summaries (K decade^{-1}).

	Global (75°S–75°N)	SXT (75°–30°S)	Tropics (30°S–30°N)	NXT (30°–75°N)
Complete				
RSS	0.170	0.056	0.174	0.270
UAH	0.140	0.055	0.098	0.313
HadAT	0.202	0.152	0.118	0.301
RSS	0.216	0.111	0.169	0.289
UAH	0.203	0.135	0.108	0.318
RAOBCORE 1.4	0.198	0.031	0.144	0.299
RSS	0.209	0.067	0.173	0.286
UAH	0.209	0.073	0.116	0.332
RICH	0.219	0.044	0.155	0.323
RSS	0.215	0.095	0.177	0.280
UAH	0.209	0.103	0.114	0.318
IUK	0.175	0.047	0.136	0.262
RSS	0.209	0.088	0.178	0.283
UAH	0.185	0.094	0.107	0.319

the unsampled (AW) and SRL trends to demonstrate the improvement in trend agreement that results when the SRL method is applied. We provide error bars representing 95% confidence intervals for the unsampled global satellite trends. Error estimates for smaller regions and subsampled datasets are likely to be larger. Note that because each radiosonde dataset has unique sampling, different SRL time series are constructed for each satellite–radiosonde dataset pair.

For global averages, the SRL method makes significant improvements in the agreement between both satellite datasets and all the radiosonde datasets. This is not surprising because the SRL averaging method results in a large portion of weight in the NXT region, where the satellite datasets are in good agreement. The high density of radiosonde stations in the NXT also makes it more likely that the homogenization procedures that are based on neighbor comparisons (all except RAOBCORE) are successful. The difference between trends in both global and NXT averages for all satellite and radiosonde dataset pairs are less than the stated uncertainties in these datasets.

In the tropics, the trend difference between two satellite datasets disagrees by almost 0.08 K decade^{-1}. This is a much larger difference, but it is still smaller than the 2σ uncertainty estimate for the RSS dataset alone (Mears and Wentz 2005). The tropical radiosonde trends lie between the SRL versions of the satellite trends, with RAOBCORE and RICH closer to the RSS trend, and HadAT and IUK closer to the UAH trend. The developers of both HadAT and IUK have concluded that their datasets may have trends that are too low in the tropics over the satellite period (Sherwood et al. 2008; Thorne et al. 2005b).

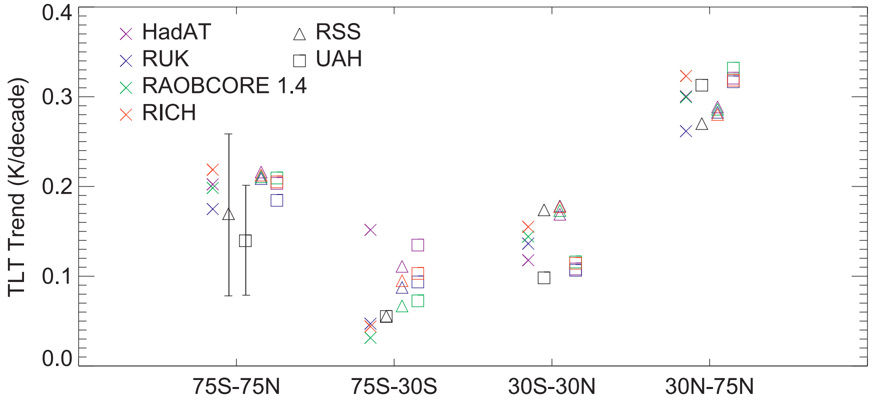

FIG. 13. Summary of TLT trends from adjusted radiosonde and satellite datasets. The colored Xs are the AW trends from radiosonde datasets, and the black symbols are the unsampled satellite trends for RSS and UAH V5.2, with error bars representing 95% confidence intervals. The colored symbols are the satellite trends found using time series calculated by sampling the satellite data only where valid radiosonde data exists. The shape of the symbol corresponds to the satellite dataset, and the color corresponds to the radiosonde dataset used for resampling.

In the SXT, the two satellite datasets are again in good agreement, particularly for spatially complete averages. The trend differences between satellite and radiosonde datasets are quite large and of varying sign. This is likely to be because the small number of radiosonde stations available in the SXT makes the radiosonde averages susceptible to unadjusted errors in individual stations. The large spatial separation between stations and/or groups of stations also makes it less likely that neighbor-based homogenization methods are successful. The southern extratropics are mostly ocean, so the satellite data should be relatively free of errors caused by errors in the adjustment for the land diurnal cycle. We conclude that the satellite data are likely to be the most accurate measurements of temperature change in the southern extratropics.

6. Conclusions

We have described the methods we used to produce a lower-tropospheric temperature dataset from measurements made by the MSU and AMSU satellites. We have attempted to remove all know sources of long-term drifts in the data so that the results can be used to evaluate decadal-scale climate change and to test the predictions of climate models. We have compared our results with those from homogenized radiosonde datasets. We find that satellite and radiosonde datasets are in good agreement when the satellite data are sampled to reflect the incomplete sampling of the radiosonde datasets. This agreement increases confidence in both the satellite and radiosonde datasets.

Acknowledgments. This work was supported by the NOAA Climate and Global Change Program Award No. NA05OAR4311111.

REFERENCES

Christy, J. R., R. W. Spencer, and W. D. Braswell, 2000: MSU tropospheric temperatures: Dataset construction and radiosonde comparisons. *J. Atmos. Oceanic Technol.,* **17,** 1153–1170.

——, ——, W. B. Norris, W. D. Braswell, and D. E. Parker, 2003: Error estimates of version 5.0 of MSU–AMSU bulk atmospheric temperatures. *J. Atmos. Oceanic Technol.,* **20,** 613–629.

Fu, Q., and C. M. Johanson, 2005: Satellite-derived vertical dependence of tropospheric temperature trends. *Geophys. Res. Lett.,* **32,** L10703, doi:10.1029/2004GL022266.

——, ——, S. G. Warren, and D. J. Seidel, 2004: Contribution of stratospheric cooling to satellite-inferred tropospheric temperature trends. *Nature,* **429,** 55–58.

Goodrum, G., K. B. Kidwell, and W. Winston, cited 2000: NOAA KLM user's guide. National Climatic Data Center. [Available online at http://www2.ncdc.noaa.gov/docs/klm/index.htm.]

Haimberger, L., 2007: Homogenization of radiosonde temperature time series using innovation statistics. *J. Climate,* **20,** 1377–1403.

——, C. Tavolato, and S. Sperka, 2008: Toward elimination of warm bias in historic radiosonde temperature records—Some new results from a comprehensive intercomparioson of upper air data. *J. Climate,* **21,** 4587–4606.

Kalnay, E., and Coauthors, 1996: The NCEP/NCAR 40-Year Reanalysis Project. *Bull. Amer. Meteor. Soc.,* **77,** 437–471.

Kidwell, K. B., cited 1998: NOAA polar orbiter data users guide. National Climatic Data Center. [Available online at http://www.ncdc.noaa.gov/oa/pod-guide/ncdc/docs/podug/index.htm.]

Kiehl, J. T., J. J. Hack, G. B. Bonan, B. A. Boville, B. P. Briegleb, D. L. Williamson, and P. J. Rasch, 1996: Description of the NCAR Community Climate Model (CCM3). NCAR Tech. Note NCAR/TN-420+STR, 152 pp.

Kursinski, E. R., G. A. Hajj, J. T. Schofield, R. P. Linfield, and K. R. Hardy, 1997: Observing Earth's atmosphere with radio occultation measurements using the global positioning system. *J. Geophys. Res.,* **102,** 23 429–23 466.

Lanzante, J. R., S. Klein, and D. J. Seidel, 2003: Temporal homogenization of monthly radiosonde temperature data. Part I: Methodology. *J. Climate,* **16,** 224–240.

Mears, C. A., and F. J. Wentz, 2005: The effect of dirunal correction on satellite-derived lower tropospheric temperature. *Science,* **309,** 1548–1551.

——, and ——, 2009: Construction of the Remote Sensing Systems V3.2 atmospheric temperature records from the MSU and AMSU microwave sounders. *J. Atmos. Oceanic Technol.,* **26,** 1040–1056.

——, M. C. Schabel, F. J. Wentz, B. D. Santer, and B. Govindasamy, 2002: Correcting the MSU middle tropospheric temperature for diurnal drifts. *Proc. Int. Geophysics and Remote Sensing Symp.,* Toronto, Canada, IGARSS, 1839–1841.

——, ——, and ——, 2003: A reanalysis of the MSU channel 2 tropospheric temperature record. *J. Climate,* **16,** 3650–3664.

Rosenkranz, P., 1993: Absorption of microwaves by atmospheric gases. *Atmospheric Remote Sensing by Microwave Radiometry,* M. A. Janssen, Ed., John Wiley and Sons, 37–90.

——, 1998: Water vapor microwave continuum absorption: A comparison of measurements and models. *Radio Sci.,* **33,** 919–928.

Sherwood, S. C., 2007: Simultaneous detection of climate change and observing biases in a network with incomplete sampling. *J. Climate,* **20,** 4047–4062.

——, C. L. Meyer, R. J. Allen, and H. A. Titchner, 2008: Robust tropospheric warming revealed by iteratively homogenized radiosonde data. *J. Climate,* **21,** 5336–5352.

Spencer, R. W., and J. R. Christy, 1992: Precision and radiosonde validation of satellite gridpoint temperature anomalies. Part II: A tropospheric retrieval and trends during 1979–1990. *J. Climate,* **5,** 858–866.

Thorne, P. W., D. E. Parker, J. R. Christy, and C. A. Mears, 2005a: Uncertainties in climate trends: Lessons from upper-air temperature records. *Bull. Amer. Meteor. Soc.,* **86,** 1437–1442.

——, ——, S. F. B. Tett, P. D. Jones, M. McCarthy, H. Coleman, and P. Brohan, 2005b: Revisiting radiosonde upper air temperatures from 1958 to 2002. *J. Geophys. Res.,* **110,** D18105, doi:10.1029/2004JD005753.

Ulaby, F. T., R. K. Moore, and A. K. Fung, 1981: *Microwave Remote Sensing: Active and Passive*. Artech House Publishers, 456 pp.

Wentz, F. J., and M. C. Schabel, 1998: Effects of satellite orbital decay on MSU lower tropospheric temperature trends. *Nature,* **394,** 661–664.

——, and T. Meissner, 2000: AMSR ocean algorithm, version 2. Remote Sensing Systems Algorithm Theoretical Basis Doc. 121599A-1, 66 pp.